Sound & Vibration 2026, 60(5), 4470.
doi: https://doi.org/10.59400/sv4470

Article

Nonlinear global dynamic characteristics and experimental validation of a cylindrical shell

Haotian Song[1], **Shufeng Lu**[1,2,*]

[1] Department of Mechanics, Inner Mongolia University of Technology, Hohhot 010051, China

[2] Key Laboratory of Civil Engineering Structure and Mechanics, Inner Mongolia University of Technology, Hohhot 010051, China

*** Corresponding author:** Shufeng Lu, sflu@imut.edu.cn

CITATION

Song H, Lu S. Nonlinear global dynamic characteristics and experimental validation of a cylindrical shell. Sound & Vibration. 2026; 60(5): 4470. https://doi.org/10.59400/sv4470

ARTICLE INFO

Received: 1 June 2026
Revised: 18 July 2026
Accepted: 23 July 2026
Available online: 25 July 2026

Abstract: Based on first-order shear deformation theory and the Rayleigh-Ritz method, this paper establishes the dynamic model for a cylindrical shell with various boundary conditions (fixed, simply supported, free or elastically supported etc.) by means of Chebyshev polynomials and the artificial boundary spring method. To validate the proposed approach, a comparative study is first conducted with existing literature, finite element simulations, and experimental modal tests. The results demonstrate that the method can accurately predict the natural frequencies and mode shapes of the shell. Subsequently, the method of multiple scales is introduced to perform a perturbation analysis of the nonlinear governing equations. Through polar coordinate transformations, the four-dimensional averaged equations of the system are derived. Finally, based on the averaged equations, the amplitude–frequency response characteristics are systematically analyzed, revealing typical nonlinear phenomena such as multi-valued solutions, jump instabilities, and softening–hardening spring behaviors. Furthermore, the Runge–Kutta algorithm is employed to obtain the bifurcation diagrams, phase portraits, Poincaré maps, and maximum Lyapunov exponents. The results indicate that the external excitation amplitude acts as the dominant parameter inducing bifurcations and chaos, whereas the detuning parameter exhibits a weakly sensitive local perturbation effect.

Keywords: cylindrical shell; bifurcation and chaos; Chebyshev polynomial; artificial boundary spring; 1:2 internal resonance

1. Introduction

Multi-field coupling dynamics modeling is a research hotspot in the nonlinear vibration of composite cylindrical shells. Many scholars have studied multi-field coupling dynamics models based on piezoelectric and functionally graded cylindrical shells. Du et al. [1] proposed a high-precision multi-field coupled dynamic model for bolted flanged cylindrical shells and piezoelectric laminated cylindrical shells by simultaneously considering the multi-field nonlinearity and the non-uniform defects of structural connections. Zhang et al. [2] established a nonlinear model of composite piezoelectric functional plate and shell and studied its nonlinear behavior. Liu et al. [3] derived the multi-field nonlinear coupling control equation of rotating cylindrical shells under multi-harmonic excitation in a thermal environment; Zhang et al. [4] verified the multi-field coupling dynamic model of piezoelectric laminated cylindrical shells based on theoretical analysis, finite element method analysis and experiments. Liu et al. [5] proposed a solution strategy to greatly simplify the difficulty of solving the vibration of functionally graded piezoelectric cylindrical shells with strong multi-field coupling. Liu et al. [6] obtained the evolution law of resonance response of a functionally gradient cylindrical shell under humid and hot environment, air pressure and external excitation. The above research has established the basic research results of multi-field coupling analysis, but the research objects and constraints are highly specific, and the model can only be applied to one structural case, without the ability to be widely apply to multi-case analysis.

On this basis, scholars began to study new functional shells such as interlayer, graphene reinforcement and coating, which further enriched the multi-field coupling system. Zuo et al. [7] proposed the variable stiffness artificial spring constraint method to solve the thermal vibration of an arbitrary boundary layer combined cylindrical shell. Zheng et al. [8] established free vibration models of multi-layer damped sandwich open shells with different lay-up angles based on first-order shear deformation shell theory. Huang et al. [9] studied the nonlinear vibration characteristics of functionally graded graphene-reinforced porous composite conical shells with axial motion. Gholami and Ghadiri [10] prepared a graphene-based graded porous composite material to improve the vibration characteristics of the structure from the material level. Ma et al. [11] obtained the dynamic behavior and instability interval of graphene-reinforced aluminum-based truncated conical shells under 1:1 internal resonance through full-parameter scanning. Li et al. [12] modeled and analyzed the influence of graphene distribution and geometric parameters on the vibration response of cone-column-cone connected shells under random loading. Subsequently, Zhu et al. [13], Du et al. [14], Zheng et al. [15], and Truong [16] respectively conducted coupling characteristic analyses for piezoelectric semiconductor laminated shells, coated ring-disk coupled shells, hard-coated thin-walled shells, and gradient porous reinforced shells. These studies are specific control equations for specific shells and cannot form a unified multi-field coupling model that is adaptable to all types of composite shells.

Concurrently, the prevalence of irregularly shaped shells in engineering practice—such as corrugated, sandwich, graded porous, and woven shells—has attracted considerable attention. Studies have demonstrated that boundary constraint forms significantly influence the dynamic behavior of cylindrical shells [17–19]. The dynamic behavior of cylindrical shells with different materials under different boundary conditions has also been studied significantly in thermal environment [20–23]. Nevertheless, a critical limitation persists: almost all such investigations are restricted to classical rigid boundary conditions, rendering them incapable of handling the elastic supports and mixed constraints commonly encountered in engineering applications. The adaptability of these models to complex boundary conditions remains markedly inadequate.

In practical engineering, cylindrical shells often appear in combination forms, such as cone column combined shells, ring rib reinforced shells, and plate shell coupling systems. The vibration analysis of coupled structures has stronger engineering value, but existing solution methods are mostly specialized solutions for specific component combinations [24–28], such as the rotating column shell plate coupling system [24], double-layer column shell ring rib coupling system [25], the discontinuous ring plate-cylindrical shell coupling system [26], the composite laminated connection cone-cylindrical shell [27], and the double-layer cylindrical shell [28]. The displacement functions and boundary value conditions of these methods are set for specific configurations and cannot be extended to coupled shell problems with any combination of components.

At the level of computational methods, scholars have developed various numerical methods such as semi-analytical methods [29], differential transformation methods [30], and spectral element methods [31, 32] to improve the accuracy and efficiency of multi-field coupling, nonlinear, and composite shell problems. Wang et al. [33] used linear springs and potential flow theory to solve the vibration response problem of liquid-filled cylindrical shells with cracks. However, these methods are independent of each other, lack intrinsic connections, are each applicable to specific types of problems, and have not yet formed a unified analytical framework. Various numerical simulation software also operate independently, making it difficult to achieve integrated solutions for multiple field loads, irregular shells, and coupled structures.

In summary, four systemic deficiencies characterize the current state of research: (1) the application scenarios of multi-field coupling models are overly narrow, with no general dynamic model capable of accommodating diverse loading conditions; (2) analytical models for special shells are restricted to conventional rigid boundaries and cannot simulate the complex elastic constraints encountered in actual engineering; (3) solution methods for coupled shells depend on structure-specific displacement functions and boundary value conditions, precluding extension to other configurations; and (4) different numerical computation methods are not interconnected, and no unified analytical model system exists.

To address these issues, this paper establishes a unified dynamic analysis model for cylindrical shells under complex boundary conditions, based on first-order shear deformation theory and the Rayleigh-Ritz method, in conjunction with Chebyshev polynomials and the artificial boundary spring technique. The core advantages of the proposed approach are threefold: the artificial spring technique enables unified treatment of various boundary constraints (including both classical and elastic boundaries); the excellent orthogonality and convergence properties of Chebyshev polynomials allow for a unified expansion of the displacement field; and these features collectively overcome the dual limitations of traditional methods regarding structural form and boundary conditions. Validation tests demonstrate that the proposed method is accurate and reliable, achieving high precision while significantly improving computational efficiency. Moreover, it is seamlessly extensible to different shell configurations and combined forms, thereby enriching the existing research landscape on nonlinear vibration problems of cylindrical shells.

The organization of the paper is as follows: Section 2 established the dynamic model for a cylindrical shell with arbitrary boundary constraints, and the natural frequencies of the system were derived theoretically. In Section 3, the natural frequencies were further examined through convergence analyses, as well as simulation and experimental validations. Section 4 focused on the dynamic analysis of the conical shell, encompassing the derivation of the system's ordinary differential equations, perturbation analysis, and global dynamic analysis. Finally, the concluding remarks were provided in the last section.

2. Natural frequency derivation

As shown in **Figure 1**, the cylindrical shell is modeled with boundary springs. The shell has length l, wall thickness h, and mid-surface radius r, with Elastic modulus E, Poisson's ratio u, and density ρ. Based on the first-order shear deformation theory, the displacement field can be expressed as follows:

$$\begin{Bmatrix} \varepsilon_x^{(0)} \\ \varepsilon_\theta^{(0)} \\ \gamma_{x\theta}^{(0)} \\ \gamma_{\theta z}^{(0)} \\ \gamma_{xz}^{(0)} \end{Bmatrix} = \begin{Bmatrix} \frac{\partial u_0}{\partial x} + \frac{1}{2}\left(\frac{\partial w_0}{\partial x}\right)^2 \\ \frac{1}{R}\frac{\partial v_0}{\partial \theta} + \frac{1}{R}w_0 + \frac{1}{2}\frac{1}{R^2}\left(\frac{\partial w_0}{\partial \theta}\right)^2 \\ \frac{1}{R}\frac{\partial u_0}{\partial \theta} + \frac{\partial v_0}{\partial x} + \frac{1}{R}\frac{\partial w_0}{\partial x}\frac{\partial w_0}{\partial \theta} \\ \varphi_\theta + \frac{1}{R}\frac{\partial w_0}{\partial \theta} - \frac{1}{R}v_0 \\ \varphi_x + \frac{\partial w_0}{\partial x} \end{Bmatrix}, \tag{1a}$$

$$\begin{Bmatrix} \varepsilon_x^{(1)} \\ \varepsilon_\theta^{(1)} \\ \gamma_{x\theta}^{(1)} \end{Bmatrix} = \begin{Bmatrix} \frac{\partial \varphi_x}{\partial x} \\ \frac{1}{R}\frac{\partial \varphi_\theta}{\partial \theta} \\ \frac{\partial \varphi_x}{\partial x} + \frac{1}{R}\frac{\partial \varphi_x}{\partial \theta} \end{Bmatrix}, \tag{1b}$$

where u, v, and w denote the displacements of an arbitrary point in the shell along the x, θ, and z directions, respectively, while ϕ_x and ϕ_θ represent the rotations of the mid-surface normal about the x axis and θ axis, respectively.

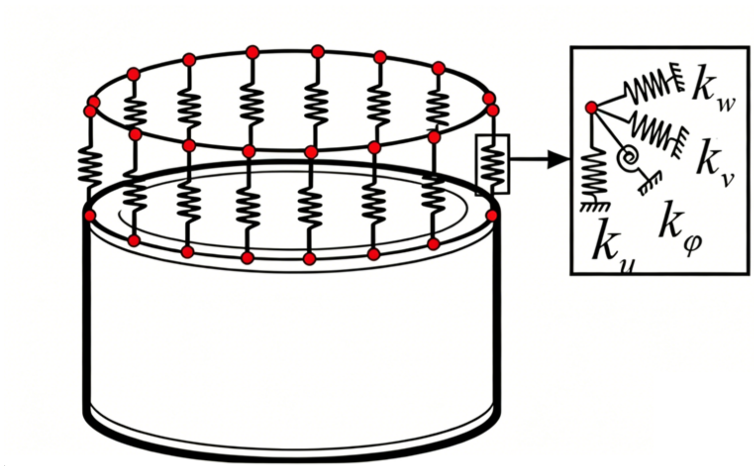

Figure 1. Boundary condition spring schematic diagram.

According to Hooke's law for linear elasticity, the normal stresses and shear stresses can be expressed, respectively, as:

$$\begin{pmatrix} \sigma_{xx} \\ \sigma_{\theta\theta} \\ \tau_{\theta z} \\ \tau_{xx} \\ \tau_{\theta x} \end{pmatrix} = \begin{pmatrix} Q_{11} & Q_{12} & 0 & 0 & Q_{16} \\ Q_{12} & Q_{22} & 0 & 0 & Q_{26} \\ 0 & 0 & Q_{44} & 0 & 0 \\ 0 & 0 & 0 & Q_{55} & 0 \\ Q_{16} & Q_{26}^{o} & 0 & 0 & Q_{66} \end{pmatrix} \begin{pmatrix} \varepsilon_{xx} \\ \varepsilon_{\theta\theta} \\ \gamma_{\theta z} \\ \gamma_{xx} \\ \gamma_{\theta x} \end{pmatrix}, \tag{2}$$

where Q_{ij} is the elastic constant matrix. For isotropic materials, these coefficients are expressed as:

$$Q_{11} = Q_{22} = \frac{E}{1-\nu^2}, \tag{3a}$$

$$Q_{12} = \frac{\nu E}{1-\nu^2}, \tag{3b}$$

$$Q_{44} = Q_{55} = Q_{66}. \tag{3c}$$

The expressions of internal force N, internal moment M and shear force are as follows:

$$\begin{Bmatrix} N_{xx} \\ N_{\theta\theta} \\ N_{x\theta} \end{Bmatrix} = [A] \begin{Bmatrix} \varepsilon_{xx}^{(0)} \\ \varepsilon_{\theta\theta}^{(0)} \\ \gamma_{x\theta}^{(0)} \end{Bmatrix} + [B] \begin{Bmatrix} \varepsilon_{xx}^{(1)} \\ \varepsilon_{\theta\theta}^{(1)} \\ \gamma_{x\theta}^{(1)} \end{Bmatrix}, \tag{4a}$$

$$\begin{Bmatrix} M_{xx} \\ M_{\theta\theta} \\ M_{x\theta} \end{Bmatrix} = [B] \begin{Bmatrix} \varepsilon_{xx}^{(0)} \\ \varepsilon_{\theta\theta}^{(0)} \\ \gamma_{x\theta}^{(0)} \end{Bmatrix} + [D] \begin{Bmatrix} \varepsilon_{xx}^{(1)} \\ \varepsilon_{\theta\theta}^{(1)} \\ \gamma_{x\theta}^{(1)} \end{Bmatrix}. \tag{4b}$$

The transverse forces in the x axis and θ axis directions are Q_x and Q_θ:

$$\begin{Bmatrix} Q_\theta \\ Q_x \end{Bmatrix} = K_s \begin{bmatrix} A_{44} & A_{45} \\ A_{45} & A_{55} \end{bmatrix} \begin{Bmatrix} \gamma_{\theta z} \\ \gamma_{xz} \end{Bmatrix}, \tag{4c}$$

where κ is the shear correction factor, which is typically taken as:

$$A_{ij} = Q_{ij}(z_k - z_{k-1}) = \int_{-\frac{h}{2}}^{\frac{h}{2}} Q_{ij} dz, \quad (i,j=1,2,6), \tag{5a}$$

$$B_{ij} = \frac{1}{2} Q_{ij}(z_k^2 - z_{k-1}^2) = \int_{-\frac{h}{2}}^{\frac{h}{2}} Q_{ij} z dz, \quad (i,j=1,2,6), \tag{5b}$$

$$D_{ij} = \frac{1}{3} Q_{ij}(z_k^3 - z_{k-1}^3) = \int_{-\frac{h}{2}}^{\frac{h}{2}} Q_{ij} z^2 dz, \quad (i,j=1,2,6). \tag{5c}$$

The variation of the strain energy U, the variation of the kinetic energy K, and the virtual work W done by external forces on the system are expressed, respectively, as:

$$\begin{aligned} U_S &= \tfrac{1}{2} \textstyle\int_V N_{xx}\varepsilon_x^{(0)} + M_{xx}\varepsilon_x^{(1)} + N_{\theta\theta}\varepsilon_\theta^{(0)} + M_{\theta\theta}\varepsilon_\theta^{(1)} \\ &\quad + Q_{\theta z}\gamma_{\theta z}^{(0)} + N_{x\theta}\gamma_{x\theta}^{(0)} + M_{x\theta}\gamma_{x\theta}^{(1)} + Q_{xz}\gamma_{xz}^{(0)} \mathrm{dV} \end{aligned}, \tag{6a}$$

$$\begin{aligned} U_K &= \textstyle\int_0^{2\pi} \left(k_{u0}\left(u_0\right)^2 + k_{\nu 0}\left(v_0\right)^2 + k_{w0}\left(w_0\right)^2 + k_{\varphi_{x0}}\left(\varphi_{x0}\right)^2 + k_{\varphi_{\theta 0}}\left(\varphi_{\theta 0}\right)^2 \right)_{x=0} R\mathrm{d}\theta \\ &\quad + \textstyle\int_0^{2\pi} \left(k_{uL}\left(u_0\right)^2 + k_{vL}\left(v_0\right)^2 + k_{wL}\left(w_0\right)^2 + k_{\varphi_{xL}}\left(\varphi_{x0}\right)^2 + k_{\varphi_{\theta L}}\left(\varphi_{\theta 0}\right)^2 \right)_{x=L} R\mathrm{d}\theta \end{aligned}, \tag{6b}$$

$$K = \frac{1}{2} \int_0^{2\pi} \int_0^L \int_{-\frac{h}{2}}^{\frac{h}{2}} \rho^{(k)} \left((\dot{u})^2 + (\dot{v})^2 + (\dot{w})^2 \right) R dz dx d\theta, \tag{6c}$$

$$\begin{aligned} W &= \frac{1}{2}\int_0^{2\pi}\int_0^L P\left(\frac{\partial w_0}{\partial x}\right)^2 \mathrm{d}x\mathrm{d}\theta + \frac{1}{2}\int_0^{2\pi}\int_0^L Fw_0 R\mathrm{d}x\mathrm{d}\theta \\ &-\frac{1}{2}\int_0^{2\pi}\int_0^L \left(k_n\dot{w}_0 - \Delta P\right) w_0 R\mathrm{d}x\mathrm{d}\theta \end{aligned}, \tag{6d}$$

$$U = U_S + U_K, \tag{6e}$$

where k_n is the damping coefficient, ρ is the mass density, and the '.' represents the time derivative. The in-plane load is $P = P_0 + P_a\cos(\omega t)$, with P_0 and P_a being the amplitudes of its static and dynamic parts. The transverse harmonic excitation is $F = F_a\cos(\omega t)\,(\sin(n\theta) + \cos(n\theta))$, where F_a is the amplitude and ω is the excitation frequency.

$$I_i = \sum\nolimits_{k=1}^{N} \int_{z_{(k-1)}}^{z_{(k)}} \rho^{(k)}(z)^{(i)} dz, \qquad (i = 0, 1, 2), \tag{7}$$

where $z_{(k)}$ and $z_{(k-1)}$ are the coordinates of the upper and lower surfaces of the k-th layer, respectively.

The vibration problem of cylindrical shells should be investigated from the perspective of traveling wave vibration. To this end, the circumferential displacement is described using trigonometric functions, while the modal functions along the x direction are solved via Chebyshev polynomials. Based on this, the five displacement components on the mid-surface can be expressed as:

$$u_0 = \sum\nolimits_{m=1}^{M} \sum\nolimits_{n=1}^{N} u_{mn}(t) X_m^{(u_0)}(\xi) cos(n\theta), \tag{8a}$$

$$v_0 = \sum\nolimits_{m=1}^{M} \sum\nolimits_{n=1}^{N} v_{mn}(t) X_m^{(v_0)}(\xi) cos(n\theta), \tag{8b}$$

$$w_0 = \sum\nolimits_{m=1}^{M} \sum\nolimits_{n=1}^{N} w_{mn}(t) X_m^{(w_0)}(\xi) cos(n\theta), \tag{8c}$$

$$\varphi_{x0} = \sum\nolimits_{m=1}^{M} \sum\nolimits_{n=1}^{N} \varphi_{xmn}(t) X_m^{(\varphi_{x0})}(\xi) cos(n\theta), \tag{8d}$$

$$\varphi_{\theta 0} = \sum\nolimits_{m=1}^{M} \sum\nolimits_{n=1}^{N} \varphi_{\theta mn}(t) X_m^{(\varphi_{\theta 0})}(\xi) cos(n\theta), \tag{8e}$$

where $\xi = (\frac{2x}{L} - 1)$ represents the coordinate transformation from x to ξ. The Chebyshev polynomials are orthogonal over the interval $(-1, 1)$. The letter n denotes the circumferential wavenumber. The term $X_m^{(n)}(\xi) = (a = u_0, v_0, w_0, \varphi_x, \varphi_y)$ represents the Chebyshev polynomials, which are specifically expressed as follows:

$$X_m^a = 1,\ X_2^a = \xi,\ X_m^a = 2\xi X_{m-1}^a - X_{m-2}^a\ (m \geq 3). \tag{9}$$

By substituting Equations (8) and (9) into Equation (10) using the Rayleigh-Ritz method, the algebraic equation is obtained:

$$\frac{\partial \prod}{\partial q} = 0, \tag{10}$$

where

$$\prod = Umax_{max}, \tag{11}$$

$$q = \left(u_{mn}, v_{mn}, w_{mn}, \varphi_{xmn}, \varphi_{\theta mn}\right)^T. \tag{12}$$

To solve the modal and frequency of the shell, ignoring the nonlinear term in the equation, the characteristic equation matrix is obtained by solving the homogeneous linear algebraic Equation (13).

$$M\ddot{q} + (C)\dot{q} + (K_s + K_f)q = 0, \tag{13}$$

where C is the structural damping matrix, K_s and K_f are the structural stiffness matrix and the aerodynamic stiffness matrix, and M is the mass matrix.

We can also equivalently transform the above system of linear equations into a standard eigenvalue problem of the following form:

$$\mathrm{AX} = \Omega X, \tag{14}$$

where X and Ω are the eigenvectors and eigenvalues of Equation (14), where $X = [q\ \dot{q}]$ and matrix A can be written as:

$$\mathrm{A}=\begin{bmatrix} 0 & I \\ -\mathrm{M}^{-1}K & -\mathrm{M}^{-1}C \end{bmatrix}. \tag{15}$$

The resulting complex eigenvalues are expressed as $\Omega = \Omega_R + i\omega$, where the real part Ω_R represents the damping characteristic and the imaginary part ω is the natural frequency.

3. Natural frequency validation

3.1. Convergence study

To verify the reliability of the Chebyshev polynomial-based modal functions and the accuracy of the theoretical and numerical analyses of cylindrical shell vibration under various boundary conditions, the natural frequencies obtained in this study are first compared with those reported in the literature [34]. **Table 1** presents a comparison of the calculated natural frequencies for cylindrical shells with different material properties, where (m, n) denote the circumferential and axial wave numbers, respectively, corresponding to each vibration mode. As shown in the table, the first four natural frequencies obtained from the proposed method agree closely with the reference data, with the maximum relative error being approximately 0.1%. This level of consistency demonstrates the reliability of the present theoretical formulation and numerical solution procedure, providing a credible basis for the subsequent nonlinear dynamic analysis.

Table 1. Frequency comparison of the first five modes.

Document/Mode	1	2	3	4
Text (m,n)	1,766.56 Hz (5,1)	1,822.76 Hz (4,1)	2,278.53 Hz (3,1)	3,221.76 Hz (2,1)
Dong et al. [34]	1,767.41 Hz	1,821.56 Hz	2,277.40 Hz	3,219.95 Hz

The material and geometric parameters of the cylindrical shell adopted in the computations are: Elastic modulus is $E = 70$ GPa, Poisson's ratio is $\nu = 0.3$, density is $\rho = 2720$ kg/m^3, radius is $r = 0.1$ m, length is $L = 0.2$ m, and thickness is $h = r/50$.

The convergence behavior of the proposed numerical method is analyzed by computing the first eight natural frequencies as functions of the truncation order M, and the results are shown in **Figure 2a**. It can be observed that the modal frequencies decrease rapidly and then gradually become stable as M increases. Significant discrepancies appear when M ranges from 3 to 5, indicating that low truncation orders are insufficient to accurately approximate the displacement field. When M is further increased, the frequency curves tend to become nearly flat, suggesting that the numerical solutions have reached a stable convergence state for the representative model considered. To further verify the applicability of the selected truncation order under different boundary conditions, an additional convergence analysis is carried out for the first natural frequency under C–F, S–S, C–C and F–F boundary conditions, as shown in **Figure 2b**. The results indicate that the convergence behavior is affected by the boundary constraint. For the F–F and S–S boundary conditions, the first natural frequency remains almost unchanged with increasing M, showing good convergence even at relatively low truncation orders. For the C–F boundary condition, slight fluctuations are observed at low truncation orders, but the frequency becomes relatively stable as M increases. For the C–C boundary condition, the first natural frequency changes significantly when M is small, especially at M = 3 and M = 4, and then approaches a stable range when M is further increased. This demonstrates that strongly constrained boundary conditions require a sufficiently high truncation order to ensure reliable modal approximation. Accordingly, M = 8 is adopted in the subsequent calculations as a compromise between computational accuracy and efficiency for the representative boundary conditions and the low-order modes mainly discussed in this work. It should be emphasized that this truncation order is not intended to be a universal value for all possible boundary conditions or all higher-order modes. For higher-order modal analyses, different geometric parameters, or more complex elastic boundary conditions, an independent convergence verification should still be performed before determining the appropriate truncation order.

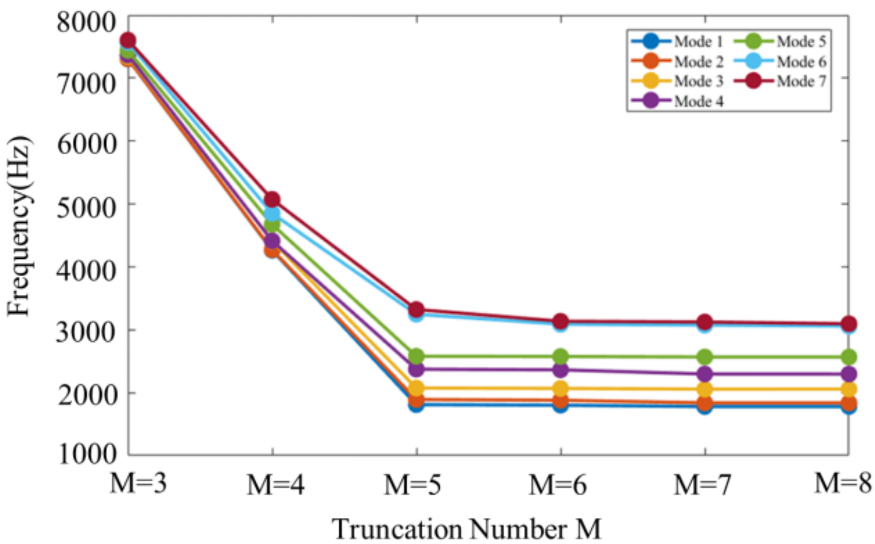

(a)

Figure 2. *Cont.*

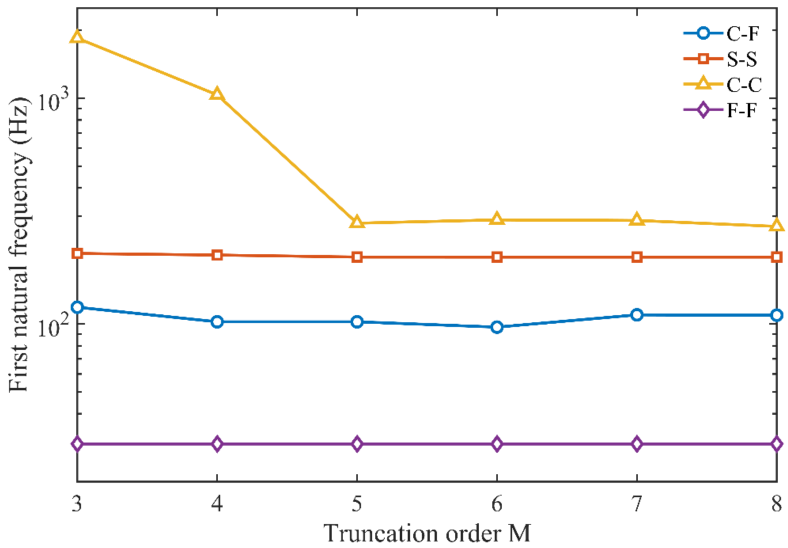

(b)

Figure 2. Convergence analysis of natural frequencies with respect to the truncation order M: **(a)** convergence curves of the first eight natural frequencies for the representative model; **(b)** convergence of the first natural frequency under different boundary conditions.

The artificial boundary spring method has been used in this paper to model several boundary conditions such as clamped, simply supported, and free boundaries. The method has the ability to implement the same boundary conditions with varying spring stiffness parameters thus ensuring both high computational efficiency and accuracy in the boundary condition approximation. To check the credibility of this method, a convergence test is carried out to progressively increase the spring stiffness up to 10^{14} N/m.

Figure 3 illustrates the evolution of the first five natural frequencies as the boundary spring stiffness parameter index b increases. As clearly observed, the curves exhibit a distinct three-stage behavior. When the spring stiffness is $b < 5$, the system approximates a free boundary condition, resulting in high-frequency rigid-body modes, and the frequencies remain constant. As b increases from 6 to 8, the boundary condition transitions from a near-free state to a clamped state. Due to this fundamental shift in physical boundary constraints—from global rigid-body motion to local elastic bending—the natural frequencies experience a sharp drop. Once the spring stiffness is $b \geq 9$, the boundary condition becomes fully saturated as a clamped constraint. At this stage, the frequencies converge to constant lower values, and further increases in stiffness no longer affect the system's dynamic behavior. This confirms the convergence and reliability of the artificial boundary spring method for simulating rigid constraints.

By defining translational and rotational stiffness separately, **Table 2** summarizes the spring stiffness values corresponding to various classical boundary conditions. k_u, k_v, and k_w represent the axial, circumferential, and radial translational spring stiffness respectively. $k_{\varphi x}$ and $k_{\varphi\theta}$ represent the axial and circumferential rotational spring stiffness. According to the artificial boundary spring method, the strength of the constraint is simulated by the magnitude of the spring stiffness: when the stiffness is 10^{13} N/m, it is approximately regarded as an equivalent rigid constraint, completely restricting the displacement and rotation. When the stiffness is 0 N/m, it indicates no constraint and complete freedom. A stiffness of 10^5 N/m is the elastic condition when the moderate stiffness is used for the simulation, allowing the structure to produce finite deformation. Therefore, E_1 is defined as three translational directions being completely rigidly constrained, and only two rotational directions adopt elastic boundaries. E_2 is axial and circumferential translational being elastic constraints, while radial translational and the two rotational directions maintain rigid constraints. E_3 is all translational and rotational directions adopting medium elastic stiffness, representing a fully elastic boundary.

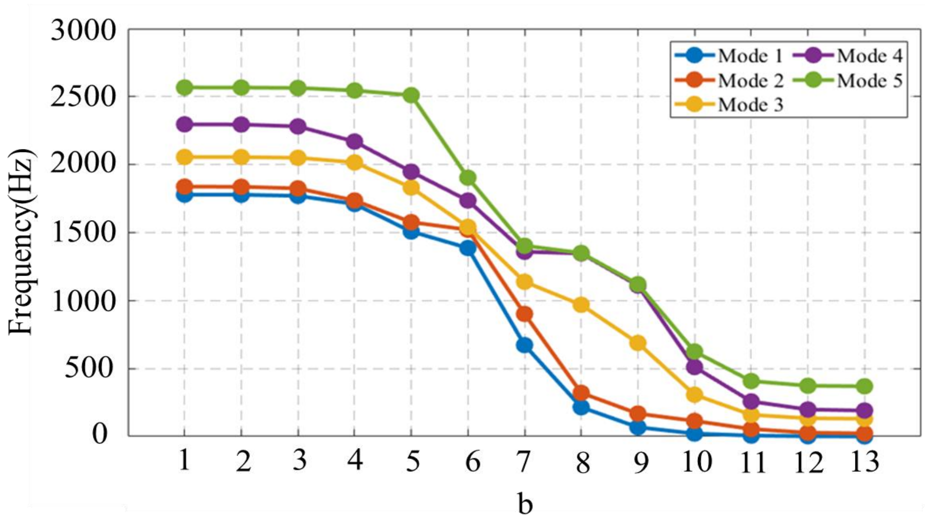

Figure 3. Diagram of the natural frequency convergence and modal response of the system with artificial boundary spring stiffness.

Table 2. Values of the spring stiffness and its boundary conditions.

BC	k_u	k_v	k_w	$k\varphi_x$	$k\varphi_\theta$
C	10^{13}	10^{13}	10^{13}	10^{13}	10^{13}
S	0	10^{13}	10^{13}	0	10^{13}
F	0	0	0	0	0
E_1	10^{13}	10^{13}	10^{13}	10^5	10^5
E_2	10^5	10^5	10^{13}	10^{13}	10^{13}
E_3	10^5	10^5	10^5	10^5	10^5

Figure 4 presents the first five natural frequencies of the cylindrical shell under different boundary conditions. The results show that stronger boundary constraints lead to higher natural frequencies, with the highest frequencies observed under clamped–clamped and elastically supported boundaries, and the lowest under the free–free boundary. For all boundary conditions, the natural frequencies increase with the mode number. The influence of boundary constraints is much more pronounced on lower-order modes than on higher-order modes, and the frequency differences between different boundary conditions gradually decrease as the mode order increases.

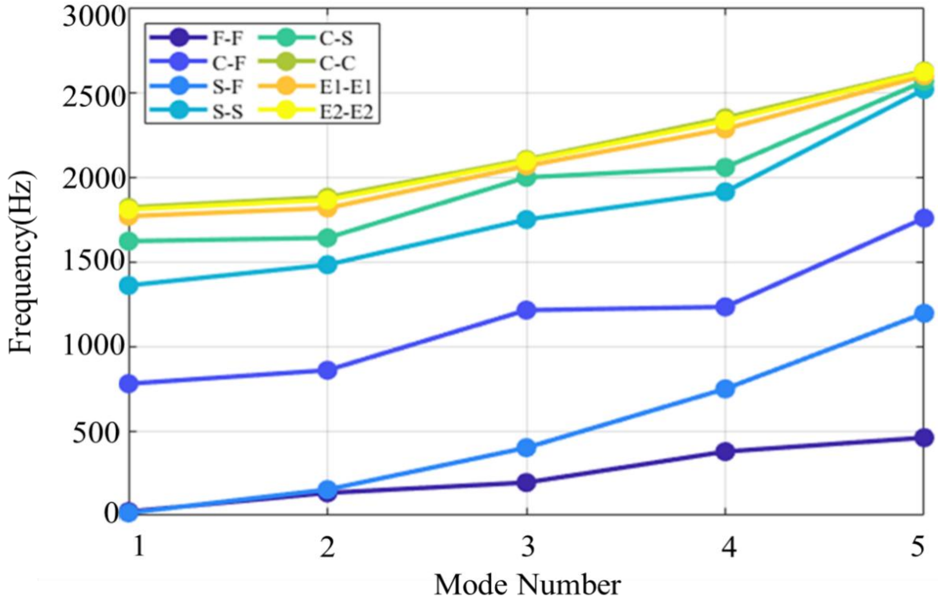

Figure 4. Comparison of natural frequencies of cylindrical shells under different boundary conditions.

3.2. Experimental and numerical simulation validations

To evaluate the reliability of the theoretical predictions, the natural frequencies and mode shapes are validated using both numerical simulations and experimental tests. The geometry of the shell used in the numerical example can be defined in the following way: shell thickness $h = 0.1$ mm, shell length $l = 800$ mm, and radius $r = 150$ mm. The remaining material parameters are listed in **Table 3**.

Table 3. Material properties table.

Mode	Simulation (Hz)	Present (Hz)	Experiment (Hz)	Simulation difference (%)	Test difference (%)
1	110.226 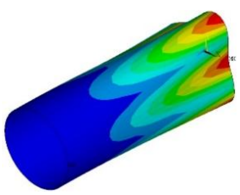	105.53 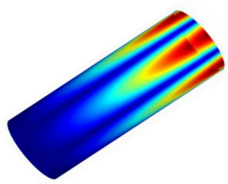	105.5 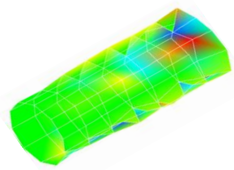	4.45	0.03
2	147.35 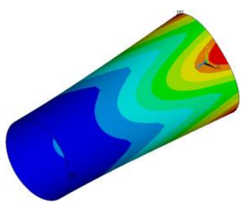	153.53 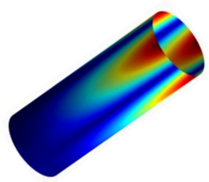	152.5 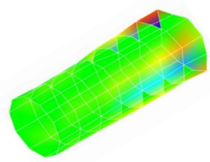	4.03	0.68
3	167.395 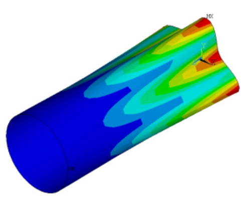	164.08 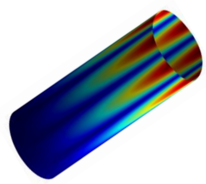	166.5 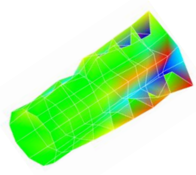	2.02	1.45

Figure 5 illustrates the experimental modal measurement system, which comprises an impact hammer, a test cylindrical shell, a mobile workstation, and a data acquisition front-end. During the experiment, the shell is welded onto a flat thin plate and then fixed to the base with threaded flanges to achieve the required boundary constraint conditions. The experimental boundary is implemented using a welded–bolted composite support structure, rather than an ideal fixed boundary in the mathematical sense. The lower circumferential edge of the cylindrical shell is continuously welded to a flat annular support plate. The girth weld primarily ensures displacement compatibility between the shell edge and the support plate and suppresses relative sliding and separation at the interface. The annular support plate is connected to the rigid test base through uniformly distributed pre-tensioned bolts and a threaded flange. The bolts do not directly constrain the thin-walled cylindrical shell; instead, they transmit the forces and bending moments carried by the welded support plate to the rigid base, while also restraining the overall rigid-body motion of the shell—support plate assembly. Therefore, the weld mainly provides local continuous connection between the shell and the support plate, whereas the bolted connection primarily provides the overall constraint between the support plate and the test base. The equivalent stiffness of the experimental boundary is collectively determined by factors such as the local flexibility of the weld, deformation of the annular support plate, bolt pre-tension, contact interface flexibility, and test base stiffness. Owing to the use of continuous circumferential welding in this experiment and the relatively high stiffness of the welded connection, this combined boundary can be approximately regarded as a quasi-fixed boundary. In the theoretical model, a value of $10^{13}\ N/m$ is adopted to characterize an ideal rigid translational constraint, thereby enabling an approximate simulation of the fixed boundary.

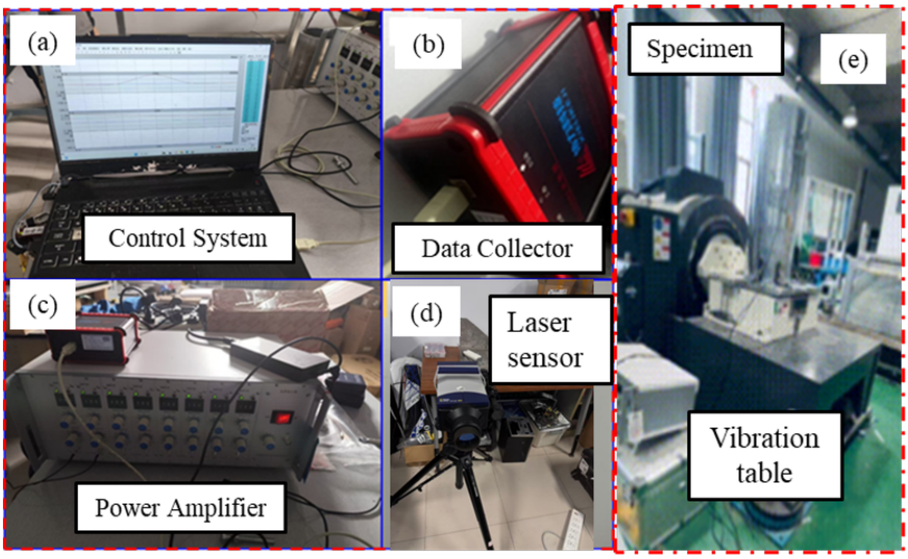

Figure 5. Testing system for impact and vibration analysis **(a)** control system; **(b)** data collector; **(c)** power amplifier; **(d)** laser sensor; **(e)** test cylindrical shell.

The sensor is attached to an appropriate position on the cylindrical shell, and the different nodes of the cylindrical shell are struck forcefully to obtain the frequency excitation of different points. The signal acquisition time is 0.001 s. Geometric modeling of the shell structure is performed within the testing system illustrated in **Figure 6**. The hammer impact method is adopted, with 70 measurement points evenly distributed on the shell surface and numbered sequentially from 1 to 70. To minimize random errors, each measurement point is struck three times by the hammer to excite the impact signal, and the sampling frequency is set to 1 kHz. The response signals captured by the acceleration sensors are acquired and stored by the data acquisition system. Following signal processing and frequency domain analysis, the frequency response functions of the structure are obtained, from which the natural frequencies and mode shapes of the shell are identified for subsequent comparison and validation with the computational results presented in this paper.

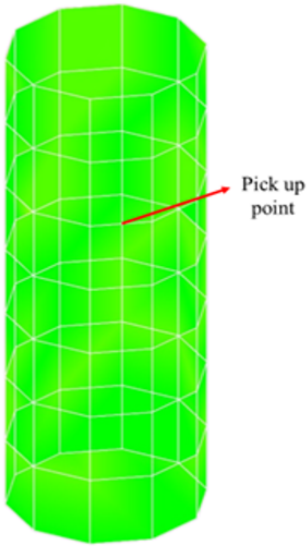

Figure 6. Model generated from experimental testing.

Table 4 presents a comparative analysis of the first three natural frequencies of the cylindrical shell, derived from the proposed theoretical model, finite element simulation, and experimental measurements, where S represents the simulation differences and T represents the experimental differences. Both the tabulated data and the visualized mode shapes reveal a remarkable consistency across the three approaches, with the relative errors for the first three natural frequencies strictly confined within a narrow range of 0.03% to 4.45%. This validates the accuracy of the theoretical derivation and the reliability of the simulation model. Furthermore, the intuitive comparison of the mode shape contours demonstrates that the deformation patterns at identical orders are homologous.

Table 4. Comparison of the calculation results of cylindrical shell materials with the experimental and simulation results.

E(GPa)	$\rho(\frac{kg}{m^3})$	ν
210	7,890	0.33

The 0.03% value in **Table 4** represents the relative error between the first-order theoretical natural frequency and the first-order experimentally identified natural frequency. The two exhibit good consistency in the first-order natural frequency, which

can be mainly attributed to the following two aspects. First, the welded annular support plate together with the pre-tensioned bolts forms a load-transfer and constraint system of relatively high stiffness, providing an effective fixed-boundary constraint effect for the overall deformation corresponding to the first-order vibration mode. Second, the first-order mode predominantly manifests as the overall deformation of the cylindrical shell. When the experimental boundary stiffness is much greater than the structural modal stiffness corresponding to this mode, the residual flexibility in the connection region has little influence on the natural frequency; therefore, the experimental results can closely approach the theoretical results under ideal fixed-boundary conditions.

The aforementioned high consistency is not universally applicable. For higher-order modes, the region near the constrained edge generally exhibits larger displacement gradients, curvature variations, and localized deformations, which may be more sensitive to weld flexibility, support plate deformation, and bolted connection flexibility. Therefore, the results of this paper merely indicate that, within the current specimen dimensions, connection configuration, and low-order modal range, the welded–bolted composite boundary can provide a reasonable approximation to the ideal fixed boundary. These findings cannot be directly generalized to other structural forms, connection parameters, or higher-order modal analyses.

4. Dynamic analysis of cylindrical shell

To systematically investigate the dynamic characteristics of the cylindrical shell, this section establishes the governing equations of motion based on Lagrange's equations. The perturbation analysis of these equations is subsequently conducted utilizing the method of multiple scales. Through coordinate transformations, the four-dimensional averaged equations of the system are derived within different coordinate frames. On this basis, both the hardening/softening spring characteristics and the global dynamic behaviors of the system are comprehensively analyzed.

4.1. Differential equation of cylindrical shell

For the nonlinear vibration problem of cylindrical shells, this paper adopts the fundamental frequency single-mode vibration model and re-deduces and corrects the expression of the mode function. The simplification strategy is based on three considerations: The 1:2 internal resonance focused on in this paper mainly involves the coupling of the first two modes, and the fundamental frequency mode is dominated by the response from low to medium excitation amplitude. The single-mode order reduction enables the multi-scale method to obtain an analytical average equation, which facilitates the analysis of basic nonlinear mechanisms such as jump, softening-hardening and chaos. Directly introducing the multimodal displacement field Equation (8) established in Section 3 will lead to a high-dimensional coupled equation system, which not only makes it difficult to analytically derive the average equation but also increases the computational cost of parameter research. Therefore, in this paper, the single-mode model is positioned as a minimization model to analyze the main nonlinear features under specific resonance conditions. Based on the above single-modal assumption, the modal functions of the five displacement components can be rewritten as follows:

$$u_0 = X_1^{u_0}(\xi)(u_1(t)cos(n\theta) + u_2(t)sin(n\theta)), \tag{16a}$$

$$v_0 = X_1^{v_0}(\xi)(v_1(t)cos(n\theta) + v_2(t)sin(n\theta)), \tag{16b}$$

$$w_0 = X_1^{w_0}(\xi)(w_1(t)cos(n\theta) + w_2(t)sin(n\theta)), \tag{16c}$$

$$\varphi_x = X_1^{\varphi_x}(\xi)(\varphi_{x1}(t)cos(n\theta) + \varphi_{x2}(t)sin(n\theta)), \tag{16d}$$

$$\varphi_\theta = X_1^{\varphi_\theta}(\xi)(\varphi_{\theta 1}(t)cos(n\theta) + \varphi_{\theta 2}(t)sin(n\theta)), \tag{16e}$$

where u_s, v_s, w_s and $\varphi_{\theta s}(s = 1, 2)$ represent time-dependent displacement functions.

According to the Lagrange equation, the motion equation is established as follows:

$$\frac{d}{dt}\left(\frac{\partial \prod}{\partial \dot{q}}\right) - \frac{\partial \prod}{\partial q} - \frac{\partial W}{\partial q} = 0, \tag{17}$$

where

$$\prod = Umax_{max},$$

$$q = (u_s, v_s, w_s, \varphi_{xs}, \varphi_{\theta s}). \tag{18}$$

Ignoring the inertial terms, the in-plane displacements (u_s, v_s) and the rotational displacements $(\varphi_{xs}, \varphi_{\theta s})$ are expressed in terms of the transverse displacement (u_s, v_s). The coupled nonlinear dynamic equations of the shell involving w_1 and w_2 are then derived as follows:

$$\begin{bmatrix} \ddot{w}_1 \\ \ddot{w}_2 \end{bmatrix} + \mu \begin{bmatrix} \dot{w}_1 \\ \dot{w}_2 \end{bmatrix} + (M+P) \begin{bmatrix} w_1 \\ w_2 \end{bmatrix} + \xi \begin{bmatrix} w_1^3 & w_1^2 w_2 & w_1 w_2^2 & w_1^3 \end{bmatrix}^T = Fcos(\varOmega\, t), \tag{19}$$

where

$$\mu = \begin{bmatrix} \mu_1 & \\ & \mu_2 \end{bmatrix}, P = \begin{bmatrix} \xi_{18} & \\ & \xi_{28} \end{bmatrix}(p_0 + p_1 cos(\varOmega\, t)), \tag{20a}$$

$$F = \begin{bmatrix} \xi_{19}F_1 & \\ & \xi_{29}F_2 \end{bmatrix}, M = \begin{bmatrix} \xi_{10} & \\ & \xi_{20} \end{bmatrix}, \tag{20b}$$

$$\xi = \begin{bmatrix} \xi_{11} & \xi_{12} & \xi_{13} & \xi_{14} \\ \xi_{21} & \xi_{22} & \xi_{23} & \xi_{24} \end{bmatrix}, \tag{20c}$$

where u_{ij} and v_{ij} are coefficients.

The dimensionless treatment is applied to Equation (19).

$$\tau = \omega_1 t, w_1 = x_1 h, w_2 = x_2 h, \quad \overline{\varOmega}_1 = \tfrac{\varOmega_1}{\omega_1}, \quad \overline{\varOmega}_2 = \tfrac{\varOmega_2}{\omega_1}, \bar{\mu}_1 = \frac{\mu_1}{\omega_1}, \bar{\mu}_2 = \frac{\mu_2}{\omega_1},$$

$$\bar{m}_{11} = \frac{m_{11}}{\omega_1^2}, \bar{n}_{21} = \frac{n_{21}}{\omega_1^2}, \bar{m}_{12} = \frac{m_{12}}{\omega_1^2}, \bar{n}_{22} = \frac{n_{22}}{\omega_1^2},$$

$$\bar{p}_1 = \frac{m_9 p_1}{\omega_1^2}, \bar{p}_2 = \frac{n_9 p_1}{\omega_1^2}, \bar{F}_1 = \frac{m_{10}F_1}{\omega_1^2 h}, \bar{F}_2 = \frac{n_{10}F_1}{\omega_1^2 h},$$

$$\overline{m}_j = \frac{m_j h}{\omega_1^2}, \quad \overline{n}_j = \frac{n_j h}{\omega_1^2}(i = 2, 3, 4), \quad \overline{m}_i = \frac{m_i h^2}{\omega_1^2}, \quad \overline{n}_i = \frac{m_i h^2}{\omega_1^2}(i = 5, 6, 7, 8). \quad (21)$$

Substituting Equation (21) into Equation (19), the dimensionless nonlinear dynamic governing equations of the first two modes are obtained as follows:

$$\ddot{x}_1 + \bar{\mu}_1 \dot{x}_1 + \bar{m}_{11} x_1 + \bar{m}_{12} x_2 + \bar{m}_2 x_1^2 + \bar{m}_3 x_1 x_2 + \bar{m}_4 x_2^2 + \bar{m}_5 x_1^3$$

$$+\bar{m}_6 x_1^2 x_2 + \bar{m}_7 x_2^2 x_1 + \bar{m}_8 x_2^3 + \bar{p}_1 cos\left(\bar{\Omega}_2 \tau\right) x_1 = \bar{F}_1 cos\left(\bar{\Omega}_1 \tau\right), \quad (22a)$$

$$\ddot{x}_2 + \bar{\mu}_2 \dot{x}_2 + \bar{n}_{21} x_1 + \bar{n}_{22} x_2 + \bar{n}_2 x_1^2 + \bar{n}_3 x_1 x_2 + \bar{n}_4 x_2^2 + \bar{n}_5 x_1^3$$

$$+\bar{n}_6 x_1^2 x_2 + \bar{n}_7 x_2^2 x_1 + \bar{n}_8 x_2^3 + \bar{p}_2 cos\left(\bar{\Omega}_2 \tau\right) x_2 = \bar{F}_2 cos\left(\bar{\Omega}_1 \tau\right). \quad (22b)$$

4.2. Multiple scale perturbation analysis

The multiple scales method is used to investigate the cylindrical shell. A small parameter ε is introduced into Equation (22), and the following transformations are made:

$$\mu_i = \varepsilon^2 \mu_i, \ p_0 = \varepsilon^2 p_0, \ F_i = \varepsilon^2 F_i, \ w_i = \varepsilon^2 w_i, \ (i = 1, 2). \quad (23)$$

For clearer subsequent descriptions, hyphens will be omitted hereinafter. Equation (19) is transformed into:

$$\varepsilon \ddot{w}_1 + \varepsilon^2 \mu_1 \dot{w}_1 + \omega_1^2 w_1 + \varepsilon m_4 w_1^3 + \varepsilon^2 m_5 w_1^2 w_2 + \varepsilon^2 m_6 w_1 w_2^2$$

$$+\varepsilon^2 m_7 w_2^3 + \varepsilon^2 m_8 w_1 p_0 cos \Omega_2 t = \varepsilon m_9 F_1 cos \Omega_1 t, \quad (24a)$$

$$\varepsilon \ddot{w}_2 + \varepsilon^2 \mu_2 \dot{w}_2 + \omega_2^2 w_2 + \varepsilon^2 n_4 w_1^3 + \varepsilon^2 n_5 w_1^2 w_2 + \varepsilon^2 n_6 w_1 w_2^2$$

$$+\varepsilon^2 n_7 w_2^3 + \varepsilon^2 n_8 w_2 p_0 cos \Omega_2 t = \varepsilon n_9 F_2 cos \Omega_1 t. \quad (24b)$$

The ratio of the first-order and second-order natural frequencies is selected as approximately 1:2. The detuning parameters σ_1 and σ_2 are introduced to describe the resonance relationship of the system as follows:

$$\Omega = \omega_2 + \varepsilon \sigma_1, \quad \omega_2 = 2\omega_1 + \varepsilon \sigma_2. \quad (25)$$

Using the multiple scales method, the approximate solutions of Equation (24) are assumed as follows:

$$w_1 = w_1^{(0)}\left(T_0, T_1, T_2\right) + \varepsilon w_1^{(1)}\left(T_0, T_1, T_2\right) + \varepsilon w_1^{(2)}\left(T_0, T_1, T_2\right), \quad (26a)$$

$$w_2 = w_2^{(0)}\left(T_0, T_1, T_2\right) + \varepsilon w_2^{(1)}\left(T_0, T_1, T_2\right) + \varepsilon w_2^{(2)}\left(T_0, T_1, T_2\right), \quad (26b)$$

in this formula $T_0 = \tau, T_1 = \varepsilon \tau, T_2 = \varepsilon^2 \tau$.

The differential operator can be expressed as:

$$\dot{w}_i = D_0 w_i^{(0)} + \varepsilon[D_0 w_i^{(0)} + D_1 w_i^{(1)}] + \varepsilon^2[D_0 w_i^{(2)} + D_1 w_i^{(1)} + D_2 w_i^{(0)}] + ... \quad (i = 1, 2), \quad (27a)$$

$$\begin{aligned}\ddot{w}_i &= D_0^2 w_i^{(0)} + \varepsilon\left[D_0^2 w_i^{(1)} + 2D_0 w_i^{(0)}\right] \\ +\varepsilon^2 &\left[D_0^2 w_i^{(2)} + 2D_0 D_1 w_i^{(0)} + D_1^2 w_i^{(0)} + 2D_0 D_2 w_i^{(0)}\right] + \ldots \quad (i=1,2)\end{aligned}, \tag{27b}$$

where $D_k = \frac{\partial}{\partial T_k},\ (k=0,1,2)$.

Substituting Equations (23) and (27) into Equation (21), and equating the coefficients of the same powers of the small parameter ε on both sides of the governing equations, the following equations can be derived:

$$\varepsilon^0$$

$$D_0^2 w_1^{(0)} + \omega_1^2 w_1^{(0)} = 0, \tag{28a}$$

$$D_0^2 w_2^{(0)} + \omega_2^2 w_2^{(0)} = 0, \tag{28b}$$

$$\varepsilon^1$$

$$D_0^2 w_1^{(1)} + \omega_1^2 w_1^{(1)} = -2D_0 D_1 w_1^{(0)} - m_3 w_1^{(0)} w_2^{(0)} + f m_9 cos(\Omega\tau), \tag{29a}$$

$$D_0^2 w_2^{(1)} + \omega_2^2 w_2^{(1)} = -2D_0 D_1 w_2^{(0)} - n_3 w_1^{(0)} - n_4 {w_2^{(0)}}^2 + f n_9 cos(\Omega\tau), \tag{29b}$$

$$\varepsilon^2$$

$$\begin{aligned}D_0^2 w_1^{(2)} + \omega_1^2 w_1^{(2)} &= -m_4 w_1^{(1)} w_2^{(0)} - \mu_1 D_0 w_1^{(0)} - 2D_0 D_1 w_1^{(1)} - \\ &2D_0 D_2 w_1^{(0)} - D_1^2 w_1^{(0)} - m_8 p_0 w_1^{(0)} cos(\Omega\tau),\end{aligned} \tag{30a}$$

$$\begin{aligned}D_0^2 w_2^{(2)} + \omega_2^2 w_2^{(2)} &= -2n_4 w_2^{(1)} w_2^{(0)} - \mu_2 D_0 w_2^{(0)} - 2D_0 D_1 w_2^{(1)} - \\ &2D_0 D_2 w_2^{(0)} - D_1^2 w_2^{(0)} - n_8 p_0 w_2^{(0)} cos(\Omega\tau).\end{aligned} \tag{30b}$$

The assumed solutions of the equations are given in the following complex form:

$$w_1^{(0)} = A_1(T_1,T_2)\, e^{i\omega_1 T_0} + \bar{A}_1(T_1,T_2)\, e^{-i\omega_1 T_0}, \tag{31a}$$

$$w_2^{(0)} = A_2(T_1,T_2)\, e^{i\omega_2 T_0} + \bar{A}_2(T_1,T_2)\, e^{-i\omega_2 T_0}, \tag{31b}$$

where $\overline{A}_1$ and $\overline{A}_2$ denote the complex conjugates of A_1 and A_2, respectively.

By eliminating the secular terms in the higher-order solutions, the following equations can be obtained:

$$2i\omega_1 \dot{A}_1 = \varepsilon(i\xi_1 A_1 + \xi_2 \bar{A}_1 e^{i(\sigma_1+\sigma_2)T_1} + \xi_3 \bar{A}_1 A_2 e^{i\sigma_2 T_1} + \xi_4 A_1^2 \bar{A}_1 + \xi_5 A_1 A_2 \bar{A}_1), \tag{32a}$$

$$2i\omega_2 \dot{A}_2 = \varepsilon(i\varsigma_1 A_1 + \varsigma_2 e^{i\sigma_1 T_1} + \varsigma_3 A_1^2 e^{-i\sigma_2 T_1} + \varsigma_4 A_2^2 \bar{A}_2 + \varsigma_5 A_1 A_2 \bar{A}_1), \tag{32b}$$

where:

$$\begin{aligned}&\xi_1 = -\omega_1\mu_1,\ \xi_2 = -\tfrac{1}{2} m_8 p_1 - \tfrac{1}{8}\tfrac{m_4 n_9 f}{\omega_1\omega_2},\ \xi_3 = -m_6,\ \xi_4 = \tfrac{2m_6 n_5}{\omega_2^2} + \tfrac{10}{3}\tfrac{m_5^2}{\omega_1^2}, \\ &\xi_5 = \tfrac{2m_7 n_6}{-\omega_1^2+2\omega_1\omega_2} + \tfrac{2m_7 n_6}{-\omega_1^2+2\omega_1\omega_2} + \tfrac{4m_5 n_7}{\omega_1^2} + \tfrac{2m_6 n_7}{\omega_2^2} + \tfrac{m_6^2}{-\omega_1^2-2\omega_1\omega_2} + \tfrac{m_6^2}{4\omega_1^2}, \\ &\varsigma_1 = -\omega_2\mu_2,\ \varsigma_2 = \tfrac{1}{2} n_9 f,\ \varsigma_3 = -n_5,\ \varsigma_4 = \tfrac{2m_7 n_6}{\omega_1^2} + \tfrac{10}{3}\tfrac{n_7^2}{\omega_2^2} + \tfrac{m_7 n_6}{\omega_1^2-4\omega_2^2} - 3n_4, \\ &\varsigma_5 = \tfrac{2m_6 n_5}{-\omega_1^2-2\omega_1\omega_2} + \tfrac{2n_6^2}{-\omega_1^2-2\omega_1\omega_2} + \tfrac{m_6 n_5}{2\omega_1\omega_2} + \tfrac{2m_5 n_6}{\omega_1^2} + \tfrac{4m_5 n_7}{\omega_2^2}.\end{aligned} \tag{33}$$

The amplitudes A_1 and A_2 can be expressed in polar coordinate form as:

$$A_1 = \frac{1}{2}a_1 e^{i\beta_1}, \quad A_2 = \frac{1}{2}a_2 e^{i\beta_2}. \tag{34}$$

Substituting Equation (34) into Equation (31), and separating the real and imaginary parts, the averaged equations of the system in polar coordinate form can be obtained.

$$\dot{a}_1 = \frac{\varepsilon}{4\omega_1}\left[2\varsigma_1 a_1 + 2\xi_2 a_1 sin\gamma_1 + \xi_3 a_1 a_2 sin(\gamma_1 - \gamma_2)\right], \tag{35a}$$

$$\dot{\gamma}_1 = \tfrac{\varepsilon}{4\omega_1}\left[4\xi_2 cos\gamma_1 + 2\xi_3 a_2 cos\left(\gamma_1 - \gamma_2\right) + \xi_4 a_1^2 + \xi_5 a_2^2 + 4\omega_1\left(\sigma_1 - \sigma_2\right)\right], \tag{35b}$$

$$\dot{a}_2 = \frac{\varepsilon}{4\omega_2}\left[2\varsigma_1 a_2 - \varsigma_3 a_2^2 sin\left(\gamma_1 - \gamma_2\right) + 4\varsigma_2 sin\gamma_2\right], \tag{35c}$$

$$\dot{\gamma}_2 = \frac{\varepsilon}{8\omega_2 a_2}\left[2\varsigma_3 a_1^3 cos\left(\gamma_1 - \gamma_2\right) + 8\varsigma_2 cos\gamma_2 + \varsigma_4 a_2^3 + \varsigma_5 a_1^2 a_2 + 8\omega_2 a_2 \sigma_1\right], \tag{35d}$$

where

$$\gamma_1 = \sigma_1 T_1 + \sigma_2 T_1 - 2\varphi_1, \gamma_2 = \sigma_1 T_1 - \varphi_2. \tag{36}$$

4.3. Amplitude–frequency and force–amplitude response curves

To quantitatively characterize the vibration characteristics of the system under different parameters, we conducted the amplitude–frequency analysis based on the averaged Equation (35).

Figure 7 shows the amplitude–frequency response curves of the shell under different values of the detuning parameter σ_1. The response curves exhibit typical nonlinear bending and multi-valued characteristics. Compared with the linear resonance response, the nonlinear resonance region is no longer represented by a single-valued smooth curve, but contains several stable and unstable solution branches. When the excitation frequency approaches the internal resonance region, the vibration amplitude increases rapidly, and an obvious jump phenomenon appears near the turning points of the response curves. This indicates that the cylindrical shell may undergo sudden transitions between low-amplitude and high-amplitude vibration states under small changes in the excitation frequency. As the detuning parameter σ_1 changes, the resonance peak and the corresponding jump position shift along the frequency axis. For smaller values of σ_1, the resonance response occurs at a relatively lower frequency, and the jump phenomenon appears earlier. With the increase of σ_1, the frequency-matching condition of the 1:2 internal resonance is modified, causing the resonance region to move and the critical amplitude corresponding to the jump phenomenon to increase. This means that the detuning parameter mainly changes the local resonance-matching condition rather than directly increasing the energy input of the system. Therefore, its influence on the global nonlinear vibration intensity is weaker than that of the external excitation amplitude.

Figure 8 presents the amplitude–frequency response curves under different external excitation amplitudes F. It can be seen that the excitation amplitude has a more significant influence on the nonlinear dynamic response than the detuning parameter.

As F increases, the resonance amplitude increases obviously, the nonlinear resonance region becomes wider, and the bending degree of the response curves becomes more pronounced. This indicates that larger external excitation introduces more energy into the shell system and enhances the nonlinear modal coupling between the first and second modes. The curves in **Figure 8** also show evident coexistence of multiple steady-state solutions. In the multi-valued frequency interval, different response amplitudes may exist under the same excitation frequency, corresponding to different stable or unstable vibration states. The turning points of the curves correspond to saddle-node bifurcation points, where the system response may jump from one stable branch to another. From the shape of the curves, the left part of the response branch shows a softening-spring characteristic, while the right part exhibits a hardening-spring characteristic. This combined softening–hardening behavior indicates that the nonlinear stiffness of the cylindrical shell is affected by both geometric nonlinearity and modal coupling under internal resonance conditions. With increasing F, the interval between the bifurcation points expands, implying that the shell is more likely to experience large-amplitude vibration, jump instability and complex nonlinear motion.

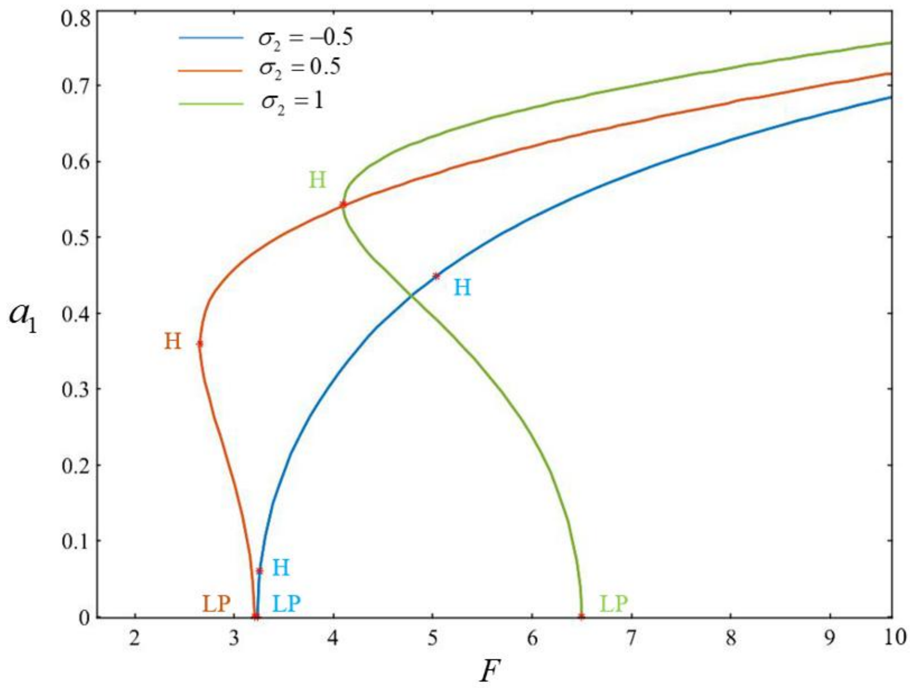

Figure 7. Amplitude–frequency response curves of the steady-state amplitude a_1 of the first-order mode of the cylindrical shell versus the external excitation amplitude F under different internal resonance detuning parameters σ_2.

Figure 9 gives the phase–frequency response curves of the shell under different external excitation amplitudes F. The phase response reflects the phase difference between the system response and the external excitation. When the excitation frequency varies across the resonance region, the phase changes continuously along the stable branches but varies sharply near the bifurcation points. This rapid phase variation indicates that the energy exchange between the external excitation and the shell vibration becomes highly sensitive in the internal resonance region.

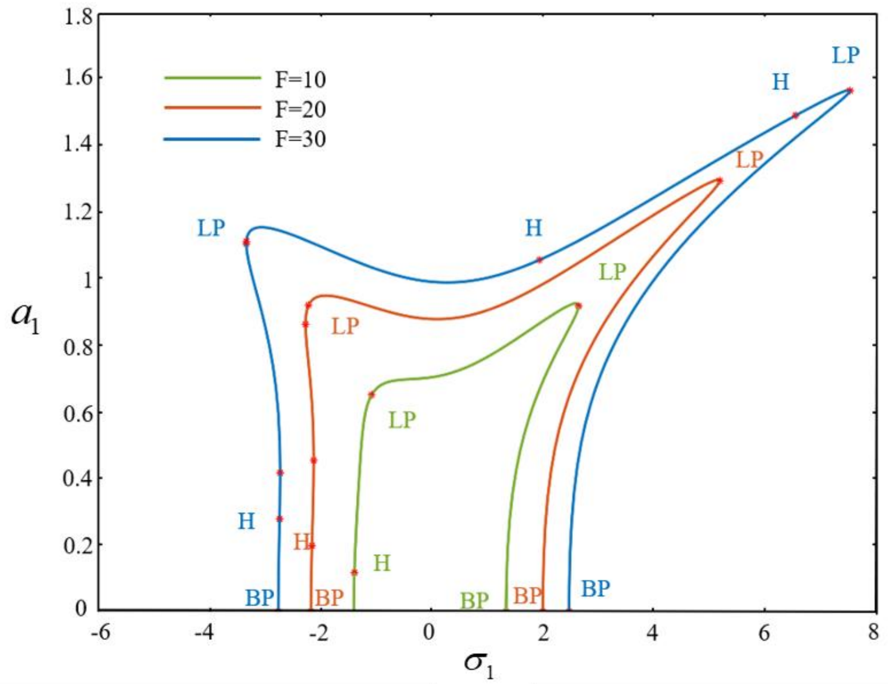

Figure 8. Amplitude–frequency response curves of the steady-state amplitude a_1 of the cylindrical shell versus the external excitation detuning parameter σ_1 under different external transverse harmonic excitation amplitudes F.

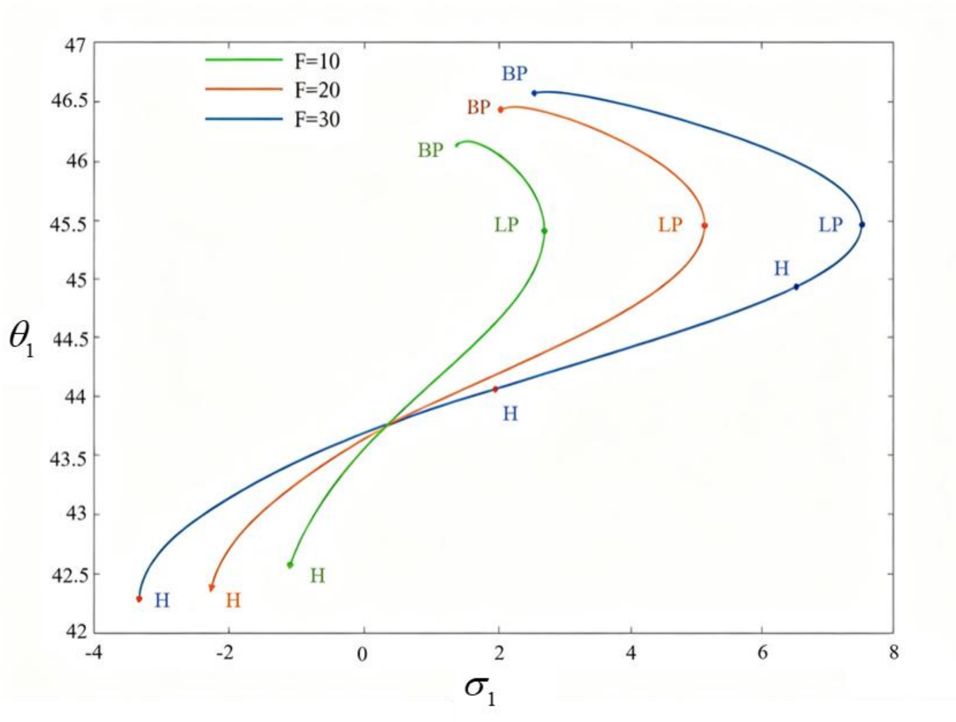

Figure 9. Phase–frequency response curves of the phase variable θ_1 of the first-order mode of the cylindrical shell versus the external excitation detuning parameter σ_1 under different external transverse harmonic excitation amplitudes F.

With the increase of F, the phase response becomes more pronounced, and the frequency interval associated with Hopf bifurcation expands. This phenomenon further confirms that the external excitation amplitude is the dominant parameter governing the nonlinear resonance behavior of the system. A larger F not only increases the response level but also promotes the loss of stability of periodic solutions.

Figures 7–9 indicate that the cylindrical shell exhibits distinct nonlinear resonance characteristics under 1:2 internal resonance conditions, including multi-valued amplitude response, jump phenomenon, softening–hardening stiffness behavior, Hopf bifurcation and stable–unstable branch transitions. The detuning parameter mainly affects the local frequency-matching condition, whereas the external excitation amplitude directly controls the energy input and has a stronger influence on the resonance amplitude, bifurcation interval and stability evolution. Therefore, reducing the excitation amplitude or avoiding the internal resonance frequency region is an effective way to suppress large-amplitude nonlinear vibration and improve the dynamic stability of cylindrical shell structures.

4.4. Nonlinear analysis of cylindrical shell

The Runge-Kutta method is adopted to solve the dimensionless governing Equation (22). Dimensionless bifurcation diagrams, maximum Lyapunov exponent diagrams, time-history curves, phase portraits and Poincaré maps are plotted to investigate the chaotic and bifurcation behaviors of the cylindrical shell under external excitations.

To investigate the influence of radial line load amplitude on the nonlinear dynamic behavior of cylindrical shells, the excitation amplitude F is adopted as the bifurcation parameter, and the bifurcation diagrams of the first two modes of the cylindrical shell system versus excitation amplitude F are plotted, where **Figure 10** shows the bifurcation diagram of the first-order mode with respect to radial load amplitude and **Figure 11** presents that of the second-order mode. It can be observed from **Figures 10** and **11** that, with an increase in the radial line load amplitude, the motion of the cylindrical shell system evolves in the sequence of periodic motion, period-doubling motion, quasi-periodic motion, chaotic motion, period-doubling motion, quasi-periodic motion, chaotic motion, and period-doubling motion. As depicted in **Figure 12**, the maximum Lyapunov exponent varies with the radial excitation amplitude F. For $0 < F < 110$, the Lyapunov exponent remains negative, indicating that the system exhibits stable periodic motion without chaotic behavior in the low-amplitude region. As the excitation amplitude increases, the exponent becomes positive over the interval $110 < F < 145$, corresponding to chaotic motion. In the range $145 < F < 160$, the exponent rapidly decreases below zero and remains temporarily negative, implying that the system transiently recovers stable periodic motion from chaos. When $160 < F < 190$, the exponent becomes positive again, and the system enters a second chaotic regime with a further increase in excitation amplitude. Finally, in the interval $190 < F < 200$, the exponent falls back to negative values and gradually stabilizes, signifying that the system restores stable periodic motion at high excitation amplitudes. Overall, the evolution of the maximum Lyapunov exponent fits well with the bifurcation plot and the corresponding dynamic response features.

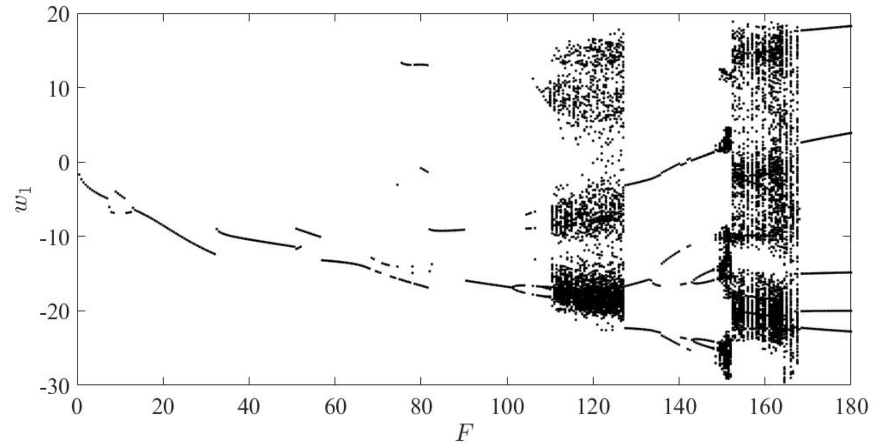

Figure 10. Bifurcation diagram of the first-order mode of radial load amplitude.

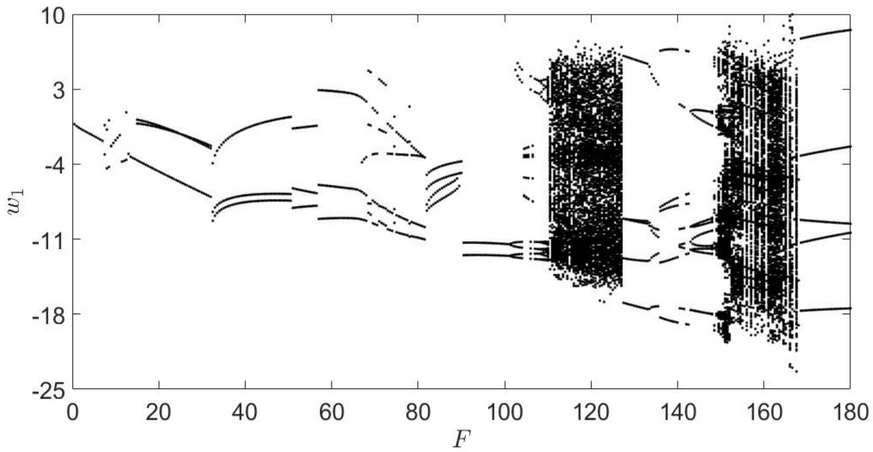

Figure 11. Bifurcation diagram of the second-order mode of radial load amplitude.

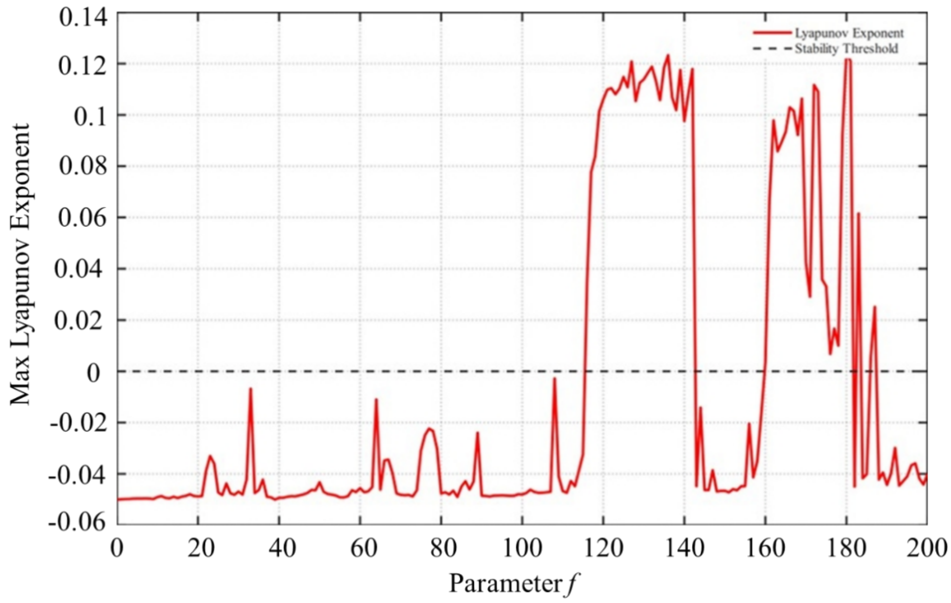

Figure 12. The curve of the maximum Lyapunov exponent changing with the radial excitation amplitude F.

To describe the corresponding dynamic behavior in detail, several representative values of transverse excitation F are selected from **Figure 13**, and the associated phase portraits, time histories, and Poincaré sections are plotted to analyze the nonlinear dynamic response characteristics under different excitation amplitudes.

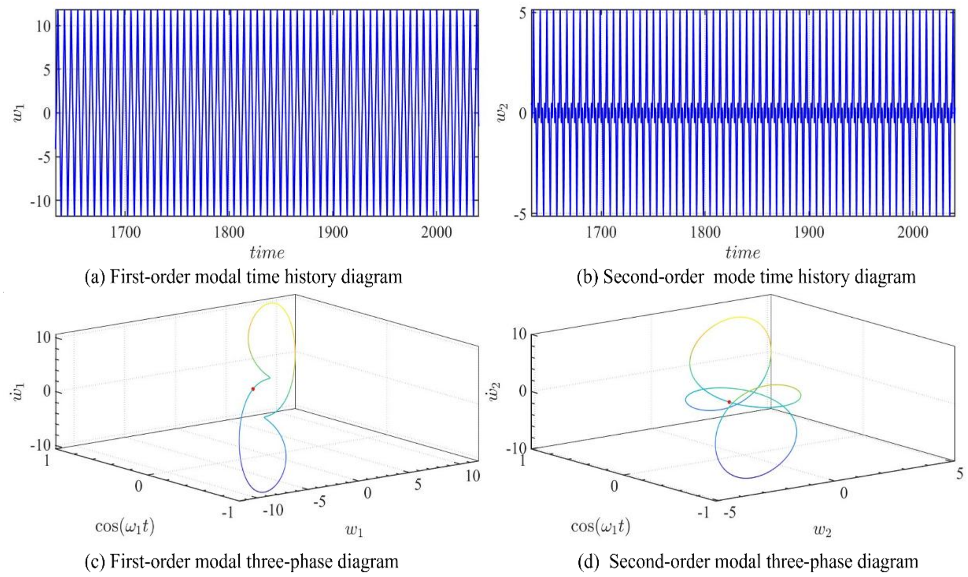

Figure 13. Single-period motion under lateral excitation F = 40.

Figure 13 illustrates the single-periodic motion of the cylindrical shell at $F = 40$. **Figure 13a,b** shows the time histories of the first- and second-order modes, respectively, revealing that the system undergoes constant-amplitude oscillations around specific fixed values of 10 and 5. These results indicate that both modes exhibit periodic motion, with the first-order mode having a higher vibration amplitude than the second. **Figure 13c,d** displays the three-dimensional phase portraits and Poincaré sections. The phase portraits feature a single closed orbit, and the Poincaré maps consist of only a solitary point, confirming that both the first- and second-order modes are undergoing single-period motion.

Figure 14 displays the dynamic response at $F = 108$. The time histories in **Figure 14a,b** shows that the system oscillates around multiple discrete values, suggesting multi-periodic motion. Specifically, **Figure 14c** demonstrates that the first-order mode undergoes period-3 motion, while **Figure 14d** indicates that the second-order mode exhibits period-5 motion.

As the excitation amplitude is further increased to $F = 146$, as shown in **Figure 15**, the system maintains multi-periodic behavior, with both the first- and second-order modes continuing to show multi-period responses. Finally, **Figure 16** depicts the dynamic response at $F = 162$. The time histories reveal that the first- and second-order modes no longer oscillate around fixed values. Moreover, the Poincaré sections display scattered sets of disordered points, which are characteristic signatures of chaotic motion. This indicates that the cylindrical shell has transitioned into a chaotic state under this high excitation level.

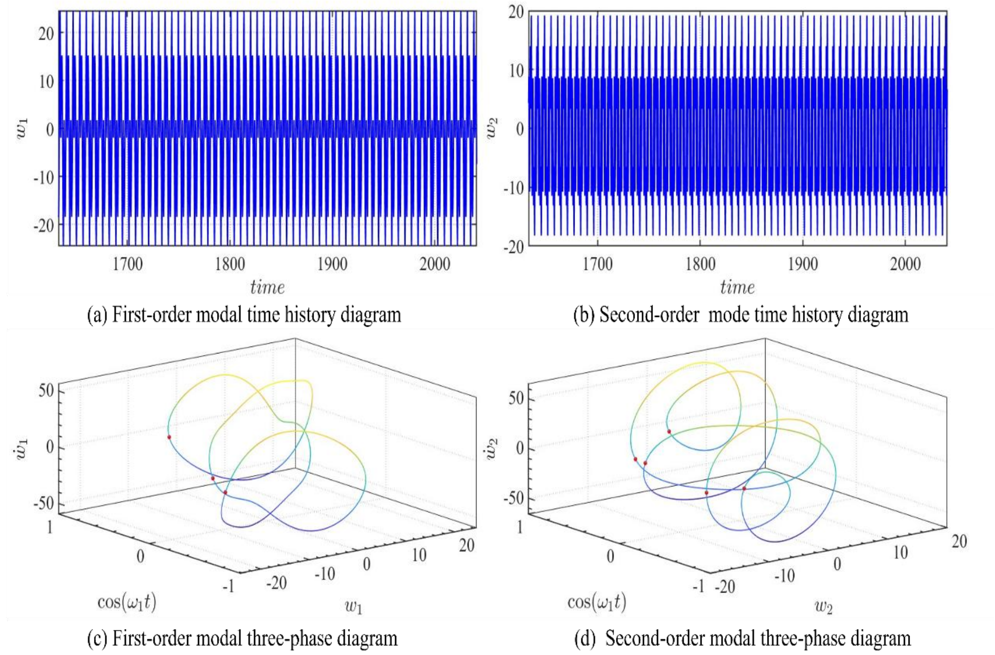

Figure 14. Multiple-period motions under lateral excitation F = 108.

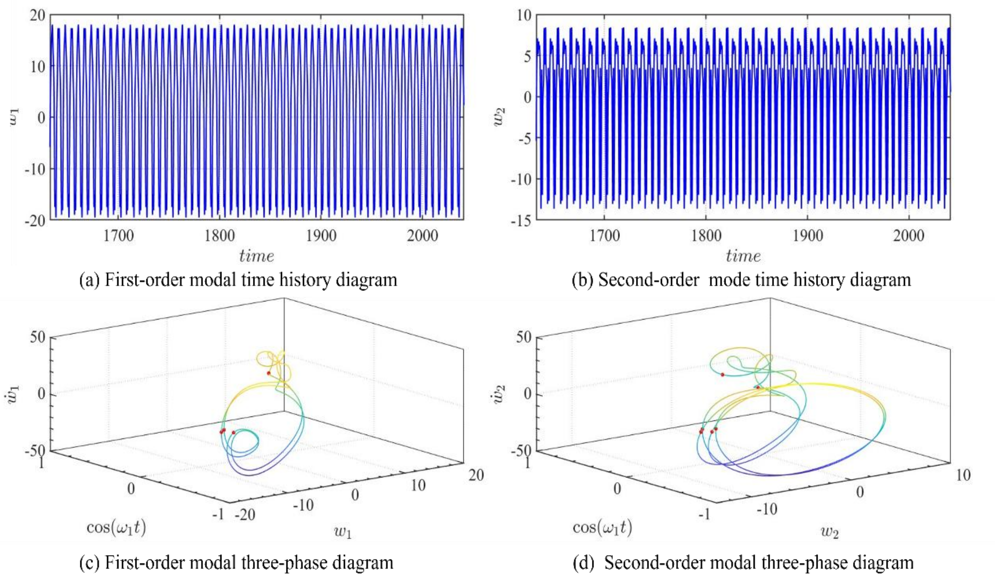

Figure 15. Multiple-period motions under lateral excitation F = 146.

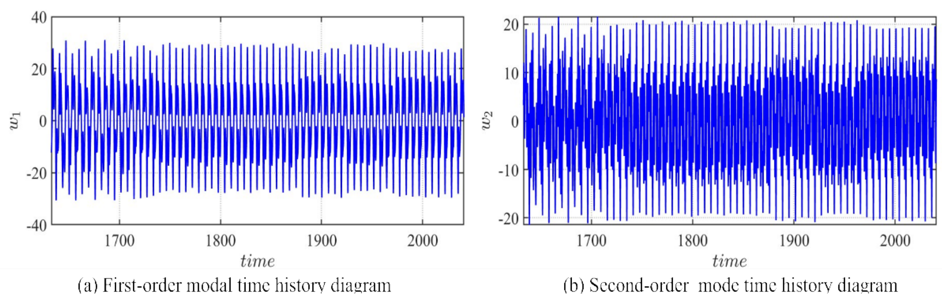

Figure 16. *Cont.*

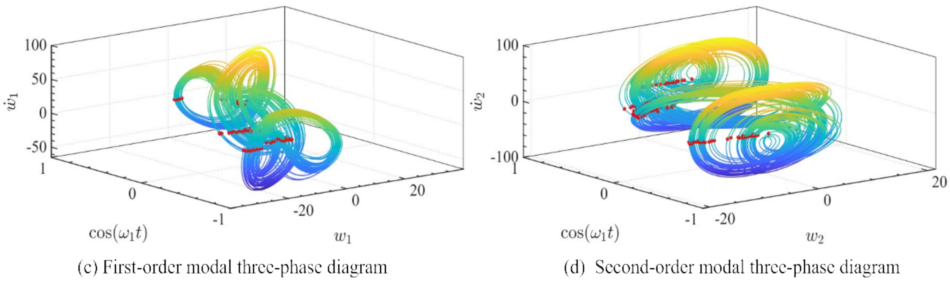

Figure 16. Chaotic motions under lateral excitation F = 162.

5. Conclusion

In this study, a dynamic model of the cylindrical shell was established based on the first-order shear deformation theory, the Rayleigh–Ritz method, Chebyshev polynomial approximations, and the artificial boundary spring technique. The accuracy and reliability of the proposed modeling approach in predicting natural frequencies were comprehensively validated through comparisons with finite element simulations and experimental modal testing. On the basis of the validated theoretical model, perturbation analysis was conducted via the method of multiple scales to derive the averaged equations, allowing for a thorough investigation of the nonlinear global dynamic characteristics under varying external excitation amplitudes and detuning parameters. The main conclusions are as follows:

(1) The Chebyshev-polynomial-based modal discretization functions can effectively approximate the displacement field of the cylindrical shell. The natural frequencies and mode shapes presented in this paper are in agreement with both finite element simulations and experimental measurements, confirming that the semi-analytical method provides a reliable numerical benchmark for the linear dynamic analysis of cylindrical shells.

(2) With the increase of excitation magnitude, the cylindrical shell exhibits an alternating occurrence of periodic and chaotic motions. The maximum Lyapunov exponent results are consistent with the dynamic evolutions observed in the bifurcation diagrams, verifying the instability process of the system.

(3) The external excitation amplitude F acts as the dominant parameter triggering bifurcation and chaos, directly altering the system's energy input and significantly affecting the resonance amplitude and stability evolution. In contrast, the circumferential wavenumbers and associated modal functions determine the natural frequencies and multimode coupling properties, acting as intrinsic structural factors influencing nonlinear vibrations. The detuning parameter σ_2, however, primarily induces local frequency-matching perturbations and is considered a weakly sensitive parameter.

Our future research aims to expand the use of modal functions related to circumferential wavenumbers by introducing high-order modes and various combinations of circumferential wavenumbers systematically instead of restricting them to the only few low-order modes that are currently used. Based on this, the emphasis will be put on the investigation of the nonlinear multimode coupled vibration properties of the cylindrical shell with different complex excitations. Additional work will focus on uncovering the nonlinear dynamics of spinning cylindrical shells with different boundary conditions, such as clamped, simply supported, free and elastic support, in order to enhance knowledge about the processes underlying multimode coupling, internal resonance, bifurcation, and chaos.

Author contributions: Conceptualization, HS and SL; methodology, HS; software, HS; validation, HS; formal analysis, HS; investigation, HS; resources, SL; data curation, HS; writing—original draft preparation, HS; writing—review and editing, HS and SL; visualization, HS; supervision, SL; project administration, SL; funding acquisition, SL. Both authors have read and agreed to the published version of the manuscript.

Funding: This work was supported by the National Natural Science Foundation of China (12172182), Natural Science Foundation of Inner Mongolia Autonomous Region (2023JQ14), Undergraduate Innovation Training Program of Inner Mongolia Autonomous Region (S202510128011), and Inner Mongolia University of Technology Student Innovation and Entrepreneurship Training Program Project (2025096006).

Institutional review board statement: Not applicable.

Informed consent statement: Not applicable.

Data availability statement: Data will be made available on request.

Conflict of interest: The authors declare no conflict of interest.

AI use statement: The authors declare that no artificial intelligence (AI) tools were used in the preparation of this manuscript.

References

1. Du D, Tian Y, Sun W, et al. Semi-analytical dynamic modeling and vibration analysis of double cylindrical shell structure based on the general bolted flange model. Engineering Structures. 2025; 333: 120027. doi: 10.1016/j.engstruct.2025.120027
2. Zhang Y, Zhu H, Zhao S, et al. Nonlinear dynamic response of functionally graded plates with piezoelectric nonlinearity. European Journal of Mechanics - A/Solids. 2025; 114: 105776. doi: 10.1016/j.euromechsol.2025.105776
3. Liu Y, Qin Z, Chu F. Nonlinear forced vibrations of rotating cylindrical shells under multi-harmonic excitations in thermal environment. Nonlinear Dynamics. 2022; 108(4): 2977–2991. doi: 10.1007/s11071-022-07449-9
4. Zhang Y, Huang Y, Zhao S, et al. Nonlinear dynamic response and stability of piezoelectric shells with piezoelectric nonlinearities. International Journal of Mechanical Sciences. 2025; 304: 110731. doi: 10.1016/j.ijmecsci.2025.110731
5. Liu Y, Qin Z, Chu F. Nonlinear forced vibrations of functionally graded piezoelectric cylindrical shells under electric-thermo-mechanical loads. International Journal of Mechanical Sciences. 2021; 201: 106474. doi: 10.1016/j.ijmecsci.2021.106474
6. Liu T, Zheng HY, Zhang W, et al. Nonlinear forced vibrations of functionally graded three-phase composite cylindrical shell subjected to aerodynamic forces, external excitations and hygrothermal environment. Thin-Walled Structures. 2024; 195: 111511. doi: 10.1016/j.tws.2023.111511
7. Zuo P, Shi X, Ge R, et al. A new meshfree approach for vibration analysis of arbitrary restrained laminated composite cylindrical shell under thermal environment. Engineering Analysis with Boundary Elements. 2022; 140: 592–606.

doi: 10.1016/j.enganabound.2022.04.028
8. Zheng C, Zhou Y, Fan Y, et al. Dynamic characteristics of novel damping sandwich composite open cylindrical shell: From theory to simulation. Thin-Walled Structures. 2024; 197: 111657. doi: 10.1016/j.tws.2024.111657
9. Huang X, Wei Y, Mo W, et al. Nonlinear Vibration Analysis of Axially Moving Truncated Porous Composite Conical Shells Reinforced with Graphene Nanoplatelets. Journal of Vibration Engineering & Technologies. 2025; 13(1): 121. doi: 10.1007/s42417-024-01626-3
10. Gholami S, Ghadiri M. Nonlinear Forced Vibration and Bifurcation Points Analysis of PFG-GPLRC Cylindrical Shell: Analysis of Internal Resonance. International Journal of Structural Stability and Dynamics. 2025; 2750041. doi: 10.1142/S0219455427500416
11. Ma W, Li D, Yang S, et al. Vibration Characteristics and Unstable Regions of a Functionally Graded GPL-Reinforced Aluminum-Based Truncated Conical Shell with 1:1 Internal Resonance. International Journal of Structural Stability and Dynamics. 2026; 26(14): 2650122. doi: 10.1142/S0219455426501221
12. Li Z, Wang Q, Yang Q, et al. Stochastic vibration behaviors of functionally graded graphene platelets reinforced composite joined conical-cylindrical-conical shell with variable taper under moving random loads. Composite Structures. 2025; 358: 118970. doi: 10.1016/j.compstruct.2025.118970
13. Zhu C, Xu Z, Liu J. Dynamic responses of a piezoelectric semiconductor sandwich cylindrical shell covered with FGPS layers. International Journal of Mechanics and Materials in Design. 2025; 21(4): 679–699. doi: 10.1007/s10999-025-09757-5
14. Du D, Sun W, Yan X, et al. Modelling and analysis of nonlinear vibrations for a coupling hard-coated ring disc-cylindric shell structure under piecewise-continuous coupling conditions. International Journal of Mechanical Sciences. 2022; 215: 106940. doi: 10.1016/j.ijmecsci.2021.106940
15. Zheng H, Zhang Y, Yang J, et al. Semi-analytical modeling and thermomechanical coupling vibration analysis of hard-coating thin-walled cylindrical shell under thermal environments and arbitrary boundary conditions. Transactions of the Canadian Society for Mechanical Engineering. 2025; 49(3): 582–595. doi: 10.1139/tcsme-2025-0029
16. Truong ND. Vibration and Buckling Analysis of Stiffened Porous Cylindrical Shell with Functionally Graded Coating under Axial Pressure. International Journal of Structural Stability and Dynamics. 2025; 2750170. doi: 10.1142/S0219455427501707
17. Liu Y, Zhu R, Qin Z, et al. A comprehensive study on vibration characteristics of corrugated cylindrical shells with arbitrary boundary conditions. Engineering Structures. 2022; 269: 114818. doi: 10.1016/j.engstruct.2022.114818
18. Dong B, Zhao R, Yu K. Nonlinear vibration of corrugated-honeycomb cylindrical shells in thermal environments. International Journal of Mechanical Sciences. 2025; 293: 110200. doi: 10.1016/j.ijmecsci.2025.110200
19. Trinh MC, Jun H. Geometrically nonlinear analysis of functionally graded composite shells using MITC4 and MITC9 elements. Thin-Walled Structures. 2023; 185: 110632. doi: 10.1016/j.tws.2023.110632
20. Zhao T, Bayat MJ, Kalhori A, et al. Free vibration analysis of functionally graded multilayer hybrid composite cylindrical shell panel reinforced by GPLs and CNTs surrounded by Winkler elastic foundation. Engineering Structures. 2024; 308: 117975. doi: 10.1016/j.engstruct.2024.117975
21. Huang Q, Gao Y, Hua F, et al. Free vibration analysis of carbon-fiber plain woven reinforced composite conical-cylindrical shell under thermal environment with general boundary conditions. Composite Structures. 2023; 322: 117340. doi: 10.1016/j.compstruct.2023.117340
22. Ebrahimi F, Mahinzare M, Rastgoo A, et al. Chaotic and nonlinear dynamic response of hybrid nanocomposite graphene origami-enabled auxetic cylindrical shell. Acta Mechanica. 2025; 236(5): 3187–3210. doi: 10.1007/s00707-025-04320-x
23. Nguyen DT, Tan NC, Yawson D, et al. Inverse problem solution and optimization in the vibration analysis of nanocomposite cylindrical shell using L-BFGS-B algorithm. Composite Structures. 2025; 370: 119309. doi: 10.1016/j.compstruct.2025.119309
24. Zhao TY, Yan K, Li HW, et al. Study on theoretical modeling and vibration performance of an assembled cylindrical shell-plate structure with whirl motion. Applied Mathematical Modelling. 2022; 110: 618–632. doi: 10.1016/j.apm.2022.06.019
25. Li Y. Free vibration analysis of double-layer thin-walled cylindrical shell–ring stiffened plate coupled structure considering welding residual stress. Thin-Walled Structures. 2025; 217: 113774. doi: 10.1016/j.tws.2025.113774
26. Liu J, Lou J, Chai K, et al. Vibration analysis of cylindrical shell discontinuously coupled with annular plate with arbitrary boundary conditions. Applied Ocean Research. 2024; 148: 104003. doi: 10.1016/j.apor.2024.104003

27. Zuo P, Shi X, Ge R, et al. Unified series solution for thermal vibration analysis of composite laminated joined conical-cylindrical shell with general boundary conditions. Thin-Walled Structures. 2022; 178: 109525. doi: 10.1016/j.tws.2022.109525
28. Wu J, Zhu H, Duan Y. Free- and Forced-Vibration Characteristic Analysis of a Double-Layered Cylindrical Shell with General Boundary Conditions. Journal of Marine Science and Engineering. 2025; 13(4): 641. doi: 10.3390/jmse13040641
29. Du Y, Tang Y, Zou Y, et al. The low frequency multi-linear spectrum vibration control study of cylindrical shell through a semi-analytical method. Thin-Walled Structures. 2024; 196: 111521. doi: 10.1016/j.tws.2023.111521
30. Khosravi AE, Shahabian F, Aftabi Sani A. Free vibration of cylindrical shells and panels with cutout via the differential transform method. Mechanics of Advanced Materials and Structures. 2024; 31(28): 10652–10670. doi: 10.1080/15376494.2023.2294494
31. Xiao X, Zhang S, Xuan J, et al. A four-node inverse curved shell element coupling MITC method for deformation reconstruction of plate and shell structures. Thin-Walled Structures. 2024; 205: 112598. doi: 10.1016/j.tws.2024.112598
32. Uspensky B, Avramov K, Malyshev S, et al. Geometrically nonlinear oscillations of composite sandwich cylindrical shell with honeycomb core under axial time periodic force. International Journal of Non-Linear Mechanics. 2025; 178: 105196. doi: 10.1016/j.ijnonlinmec.2025.105196
33. Wang T, Tan D, Hou Y, et al. Analytical and experimental investigation of vibration response for the cracked fluid-filled thin cylindrical shell under transport condition. Applied Mathematical Modelling. 2025; 142: 115969. doi: 10.1016/j.apm.2025.115969
34. Dong Y, Liu H, Hu H, et al. Semi-analytical and experimental studies on travelling wave vibrations of a moderately thick cylindrical shell subject to a spinning motion. Journal of Sound and Vibration. 2022; 535: 117095. doi: 10.1016/j.jsv.2022.117095